Journal of Engineering Science and Technology
Vol. 19, No. 1 (2024) 317 - 334

INTEGRATED ADSORPTION-PHOTOCATALYTIC DEGRADATION OF CHICKEN PROCESSING WASTEWATER USING POWDERED ACTIVATED CARBON-SUPPORTED GRAPHITIC CARBON NITRIDE

LAN CHING SIM[1,*], KEN LAP LEONG[1], WOON CHAN CHONG[1], KAH HON LEONG[2], YIK HENG CHIN[2], PICHIAH SARAVANAN[3], AZRINA ABD AZIZ[4]

[1]Department of Chemical Engineering, Lee Kong Chian Faculty of Engineering and Science, Universiti Tunku Abdul Rahman, Jalan Sungai Long 9, Bandar Sungai Long, 43000 Kajang, Selangor DE, Malaysia
[2]Department of Environmental Engineering, Faculty of Engineering and Green Technology, Universiti Tunku Abdul Rahman, Jalan Universiti, Bandar Barat, 31900 Kampar, Perak, Malaysia
[3]Environmental Nanotechnology Laboratory, Department of Environmental Science and Engineering, Indian Institute of Technology (ISM), Dhanbad, Jharkhand 826004, India
[4]Faculty of Civil Engineering Technology, Universiti Malaysia Pahang Al-Sultan Abdullah, 26300 Kuantan, Pahang, Malaysia
*Corresponding Author: simcl@utar.edu.my

Abstract

Due to the expansion of agricultural sector, a massive volume of chicken processing wastewater has been produced and the conventional technologies are ineffective to remove organic and inorganic compounds. Thus, this work investigates the performance for the adsorption-photocatalytic degradation of chicken processing wastewater using powdered activated carbon (AC) supported on different weightage of graphitic carbon nitride (g-C_3N_4) (20 wt%, 40 wt% and 60 wt%). The AC was successfully combined with g-C_3N_4 by pyrolyzing the urea and AC mixture. The presence of AC reduced the agglomeration of g-C_3N_4 by providing a larger surface area to trigger more active sites. AC achieved the highest chemical oxygen demand (COD) adsorption efficiency (79.00 %) whereas the pure g-C_3N_4 showed the strongest adsorption capacity for orthophosphate (49.10 %) and ammonia nitrogen (NH_3-N) (100 %). This proves that the microporous structure of AC was not suitable to remove orthophosphate and NH_3-N. The highest photodegradation efficiency of COD (47.00 %), orthophosphate (49.00 %) and NH_3-N (52.90 %) was successfully achieved by 20 wt% g-C_3N_4/AC, g-C_3N_4 and 60 wt% g-C_3N_4/AC, respectively. Overall, 98.20 % of COD, 98.10 % of orthophosphate and 100% of NH_3-N was removed using integrated adsorption-photocatalytic degradation, making this technique a feasible method for on-site chicken processing wastewater treatment.

Keywords: Adsorption-photocatalytic, Ammonia nitrogen, Chicken processing wastewater, COD, g-C_3N_4/AC composite, Orthophosphate.

1. Introduction

The increasing demand of chicken for human consumption contributes to the rapid growth of chicken processing industry. In Malaysia, the small scale of chicken processing industry is usually located in chicken processing stall in wet market and the untreated chicken wastewater is directly discharged into drainage system. Chicken processing effluent contains high biological oxygen demand (BOD), chemical oxygen demand (COD), phosphorus and nitrogen components like fats, oil, grease, proteins and blood [1]. Therefore, the discharge of untreated chicken effluent to drainage system can cause eutrophication [2], contamination of surface water and groundwater, and water borne diseases [3]. Conventional treatment such as biological method is a slow process and inefficient as some of the biological resistant organic compounds do not induce oxygen depletion in receiving water. Meanwhile, chemical treatment may consume large amount of chemicals to remove the undesired sludge produced and the efficiency is strongly dependent on the type of oxidants used [4].

Heterogeneous photocatalysis has been demonstrated to be a technology capable of removing COD, ammonia nitrogen (NH_3-N) and total phosphorus in real wastewater [5-7]. Goutam et al. [5] reported the use of green titanium dioxide (TiO_2) for photocatalytic treatment of tannery wastewater with 82.26% removal of COD. Li et al. [7] employed ternary g-C_3N_4/rGO/TiO_2 composite to form Z-scheme photocatalytic system for the NH_3–N removal. The obtained photocatalyst showed high NH_3–N removal efficiencies of 93.90%, 86.23% and 90.73% for coking wastewaters from different plants. He et al. [6] has proved the feasibility of using Cu/ZnO/rGO for real domestic wastewater treatment. The results showed that the removal efficiency reached 84.3, 80.7 and 90.3% for COD, total nitrogen (TN) and total phosphorus (TP), respectively. Since the results of photocatalytic application in real wastewater treatment are promising, it provides an alternative to remove the highly refractory and multi-pollutants composition in chicken processing wastewater. Further, it is suitable for on-site chicken processing wastewater treatment in the wet market as there is no secondary pollution will be generated [8] and the natural sunlight can be utilized as the energy source for photocatalysis.

Some semiconductors such as ZnO [9], TiO_2 [10], WO_3 [11] and SnO_2 [12] possess a large energy band gap which can only be energized by UV light. Besides, photocatalytic process consumes a long residence time to ensure the pollutants have been completely degraded [13]. In this context, metal-free photocatalyst g-C_3N_4 which belongs to carbon-based nanomaterials has gained much attention for its good chemical and thermal stability, low cost, moderate band gap (~ 2.7 eV) and environmentally friendly properties [14, 15]. Benefiting from its excellent visible light harvesting ability, g-C_3N_4 are widely applied in the fields of environmental remediation [16], water-splitting [17], energy conversion [18], biological and biomedical application [19]. However, g-C_3N_4 has low surface area due to the aggregated form in bulk usage which reduces the active sites for interfacial reactions, leading to low photocatalytic efficiency [20].

Aggregation of photocatalysts could be avoided by the uniform distribution of photocatalysts on the surface of a substrate such as silica [21], zeolite [22], polymers [23] and activated carbon (AC) [24]. Among the supporting substrates, AC is an efficient adsorbent for the removal of water pollutants because of its porous structure, large specific surface area, high thermal stability and variable surface chemical

composition [25, 26]. Despite the advantage of low cost and strong adsorption capacity, the adsorption sites of AC can be saturated with pollutant and thus shorten the lifetime of AC. Therefore, adsorbent and photocatalyst can be integrated in one-step adsorption-photocatalytic process to utilize the advantages of both materials such as high porosity, large surface area of adsorbent and strong oxidizing radicals of visible light-active photocatalyst. Chen et al. [27] claimed that the support of g-C_3N_4 on AC decreased the aggregation of g-C_3N_4 and increased the surface area of the composite and thus reducing the recombination rate of electron-hole pairs. The obtained composite successfully removed 100% of phenol in 160 min. Ao et al. [28] prepared TiO_2/AC using microwave-assisted heating and for the removal of tetracycline. They found that AC could act as an electron shuttle to transfer electron from TiO_2 to AC and enhanced the separation of electron-hole pairs, reaching 88% removal of tetracycline.

Numerous efforts have been done to improve the visible light absorption properties and to prolong the lifespan of charge carriers of g-C_3N_4 by coupling with other semiconductors, carbon nanomaterial and metal doping [29-31]. The results are promising but the performance is still far from satisfactory to achieve the industry scale requirement. This is because the real wastewater contains high concentration of pollutants which is hardly treated by photocatalyst with slow kinetics and low adsorption ability. The combination of adsorbent and photocatalyst provides an alternative to increase the mass transfer from the solution to adsorption sites and to reduce the release of by-products into the solution [32].

In this work, an integrated adsorption-photocatalytic system was designed to treat chicken processing wastewater which consists of highly refractory and multi-pollutants composition. Powdered activated carbon (AC) and g-C_3N_4 was employed as adsorbent and photocatalyst, respectively to fabricate a hybrid composite namely g-C_3N_4/AC. The pollutant molecules containing in the chicken processing wastewater are firstly adsorbed by AC then oxidized by the photogenerated reactive oxidizing species on the surface of g-C_3N_4. The resulting hybrid composite provided the adsorption sites for the accumulation of molecules which further underwent photodegradation under the irradiation of LED light. The novelty of this work highlights the potential of g-C_3N_4/AC to advance current approaches to real wastewater treatment. Although similar composite system was recently adopted for the removal of enrofloxacin [33] and ciprofloxacin [32], the feasibility of using such composite for real wastewater treatment containing various type of contaminants is questionable. Thus, we filled in the gap of studies by investigating the removal of COD, NH_3-N and orthophosphate in chicken processing wastewater that is rarely reported in adsorption-photocatalytic system. This represents an important knowledge gap regarding g-C_3N_4/AC as an emerging material with dual function for water remediation.

2. Materials and Methods

2.1. Chemicals

Chicken processing wastewater was collected from Sungai Long's wet market located at Kajang, Malaysia. All the chemical reagents used were of analytical grade and purity. Distilled water was used throughout the experiment. Urea powder (Merck, >99 %) was used as the precursor to synthesize g-C_3N_4 through pyrolysis method. Activated carbon powder (R&M Chemical, >99 %) was used as adsorbent

of contaminants in chicken processing wastewater. Low range chemical oxygen demand (COD) digestion reagent vials (HACH) were used to measure the amount of oxygen that is depleted in a body of receiving water by the organisms from chicken processing wastewater. Phosphate reagent powder pillow (HACH) was used to analyse the orthophosphate content in the chicken processing wastewater. Ammonium cyanurate reagent powder pillow and ammonium salicylate reagent powder pillow (HACH) were used to analyse the NH_3-N content in the chicken processing wastewater.

2.2. Synthesis of g-C_3N_4/AC composites

Firstly, urea powder was wrapped with an aluminium foil and put into an alumina crucible with a cover to avoid urea from over reacting with oxygen. The crucible was then calcinated at 550 °C in a muffle furnace (Wise Therm) for 3 h and g-C_3N_4 was then collected as pale yellowish product [16]. Then, 10 g of AC was dissolved in the 10 mL of distilled water to form AC solution. In order to prepare 20 wt% g-C_3N_4/AC composite, 2.50 g of urea powder was mixed into the AC solution. The suspension was stirred vigorously using a magnetic stirrer (HTS-1003) for 24 h under room temperature to achieve homogenous mixing. After that, the suspension was dried in an oven (Memmert) at 80 °C for overnight [33]. The dried composite was then further calcinated at 550 °C in a muffle furnace for 3 h. The procedures were repeated by varying the weight percentage of g-C_3N_4 to synthesize 40 wt% and 60 wt% g-C_3N_4/AC composites accordingly.

2.3. Characterisation

The BET (micromeritics ASAP 2020) specific surface area of the prepared composites were demonstrated by nitrogen adsorption-desorption analysis at -195.791 °C. The functional group of the prepared composites were analysed using FTIR (Nicolet iS10) spectroscopy with the wavelength in the range of 500 – 4000 cm^{-1}. Besides, the crystallite structure was analysed using XRD (Shimadzu XRD-6000) in the range of 10-80° with the rate of 2°/min. Moreover, the surface morphology and elemental composition was observed using SEM and EDX, respectively (Hitachi, S-3400N, Ametek). The zeta potentials of the prepared samples were measured using a zeta potential analyser (Malvern, Zeta Sizer Nano ZS). The powder sample was ultrasonicated in water suspension and then the zeta potential was measured in triplicate at the initial pH value.

2.4. Adsorption-photocatalytic degradation of chicken processing wastewater

The adsorption and photocatalytic performance of the synthesized catalysts were evaluated using chicken processing wastewater as model pollutant. 200 mL of chicken processing wastewater was added with 1.20 g of 20 wt% g-C_3N_4/AC. The chicken processing wastewater was then stirred magnetically and collected at every 2 h in the dark condition for 26 h to reach adsorption-desorption equilibrium. The adsorption capacity is calculated using Eq. (1):

$$\text{Adsorption efficiency (\%)} = \frac{C_0 - C_t}{C_o} \times 100\% \quad (1)$$

where: C_0 = initial concentration of pollutant before dark adsorption (mg/L) and C_t = concentration of pollutant after 26 h of dark adsorption (mg/L).

Following the dark adsorption, the beaker was then irradiated by LED light (Philips) to proceed photocatalytic process for 3 h in which each chicken processing wastewater samples were collected at every 30 min interval. Photocatalytic efficiency is calculated using Eq. (2):

$$\text{Photocatalytic efficiency (\%)} = \frac{C_0 - C_t}{C_o} \times 100\% \quad (2)$$

where: C_0 = concentration of pollutant after 26 h of dark adsorption (mg/L) and C_t = concentration of pollutant after 3 h of photocatalytic degradation (mg/L)

After photocatalytic-adsorption, the catalyst was then separated out from the treated wastewater using centrifuge (Sigma 3-18K) at 12000 rpm for 15 min. All the wastewater samples collected were analysed by carrying out COD, orthophosphate and NH_3-N test accordingly. Similar experimental procedures were repeated for AC, g-C_3N_4, 40 wt% g-C_3N_4/AC and 60 wt% g-C_3N_4/AC. The COD, orthophosphate and NH_3-N of the treated chicken processing wastewater were measured by using spectrophotometer (HACH DR 3900). COD was determined using Reactor Digestion Method (Method: 8000); orthophosphate was measured using PhosVer 3 Method (Method: 8048); while NH_3-N was measured using Salicylate Method (Method: 8155). The experiment setup for photocatalytic-adsorption process is shown in Fig. 1.

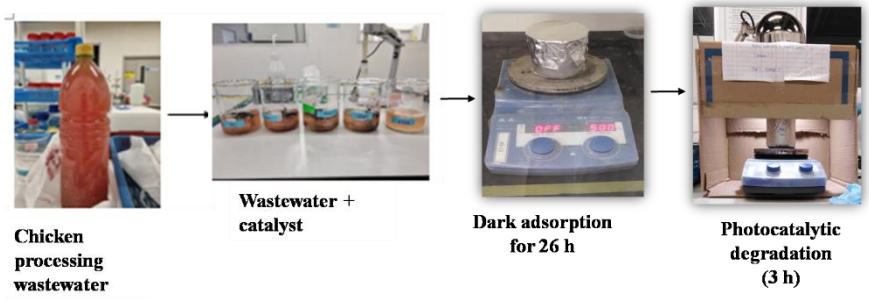

Fig. 1. Experimental setup for photocatalytic-adsorption process.

3. Results and Discussion

3.1. Brunauer-Emmett-Teller (BET) specific surface area

Table 1 shows that the specific surface area for different weight percentage of g-C_3N_4/AC composites was much larger than the bulk g-C_3N_4. This was attributed to the presence of AC which inhibited the agglomeration of g-C_3N_4 [27]. Activated carbon with higher specific surface area could act as a support catalyst to increase the surface area of g-C_3N_4 from 74.7993 m^2/g to the maximum of 1124.4379 m^2/g. The enhancement in the surface area could create more active sites for the adsorption and improved the adsorption capability of the composites for the subsequent photocatalytic reaction. Both of AC and g-C_3N_4/AC composites exhibited microporous structure with pore size less than 2 nm, while g-C_3N_4 possessed mesoporous structure with pore size of 25.3242 nm [34]. As shown in Figs. 2(a) and (b), all g-C_3N_4/AC composites exhibited type IV nitrogen sorption isotherm with an obvious hysteresis loop which is similar to AC. This shows that microporous structure of AC did not collapse or deteriorate after the addition of g-C_3N_4. The decrement of specific surface area and total pore volume with the increasing weight percentage of g-C_3N_4 in the composites suggested the

incorporation of g-C_3N_4 into the matrix of AC during pyrolysis [35]. Among the composites, 40 wt% g-C_3N_4/AC displayed the smallest pore size compared to that of 60 wt% g-C_3N_4/AC and 20 wt% g-C_3N_4/AC. This could be attributed to a higher oxidation occurred at 40 wt% g-C_3N_4/AC during thermal air oxidation in pyrolysis process. The EDX results (Table 2) support the BET data which indicate that 40 wt% g-C_3N_4/AC possess the highest atomic percent concentration of O (8.29%), followed by 20 wt% g-C_3N_4/AC (7.81%) and 60 wt% g-C_3N_4/AC (2.63%). This explains that microporous AC in 40 wt% g-C_3N_4/AC experienced more introduction of surface oxygen group during the thermal air oxidation which narrowed the entry of micropores. Hence, a lower specific surface area and smaller pore size was observed in 40 wt% g-C_3N_4/AC [36].

Table 1. BET specific surface area (S_{BET}), pore volume (V_{tot}) and pore size (D_{pore}) of AC, g-C_3N_4, 20 wt% g-C_3N_4/AC, 40 wt% g-C_3N_4/AC and 60 wt% g-C_3N_4/AC.

Catalyst	S_{BET} (m^2/g)	V_{tot} (cm^3/g)	D_{pore} (nm)
AC	1144.7041	0.5675	1.9831
g-C_3N_4	74.7993	0.4736	25.3242
20 wt% g-C_3N_4/AC	1124.4379	0.5542	1.9716
40 wt% g-C_3N_4/AC	995.1877	0.4812	1.9343
60 wt% g-C_3N_4/AC	996.4360	0.4927	1.9777

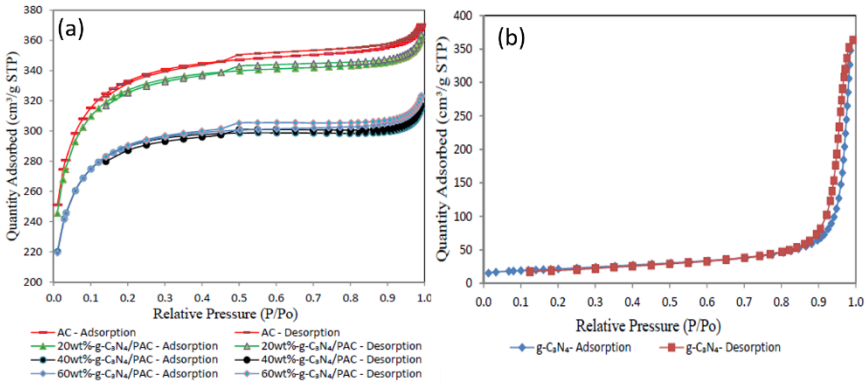

Fig. 2. N_2 adsorption isotherms of (a) AC and g-C_3N_4/AC composites and (b) g-C_3N_4.

3.2. Fourier transform infrared (FTIR) spectroscopy

In Fig. 3, the FTIR spectra of g-C_3N_4 displays a small and sharp peak located at 807 cm^{-1}. The sharp peak was arisen due to the triazine ring breathing vibration or represented as tri-s-triazine ring mode of bending [37]. Meanwhile, the small peak at 890 cm^{-1} was attributed to the deformation of cross-linked heptazine [38]. Moreover, the stretches occurred at 1232, 1314, 1400, 1458 and 1560 cm^{-1} were attributed to the aromatic C-N bonding [39, 40]. The peak at 1629 cm^{-1} was correspondent to the C=N stretching vibration mode [41]. Besides, the spectra showed the C=O and C=C bonding at around 1629–1790 cm^{-1}. The broad peak that centred at 3172 cm^{-1} was counted as the stretching mode of the N-H bond. Furthermore, g-C_3N_4/AC composites shows a similar characteristic band as g-C_3N_4 in which the C-N and C=N bonds were observed at around 1300–1560 cm^{-1}. The detection of the characteristic peaks which are C-N and C=N bonds were identified in the g-C_3N_4/AC composites

and thus; the g-C_3N_4 was said to be successfully supported on the AC. The absence of new absorption peak in the composite indicated that the g-C_3N_4/AC composite is a physical mixture and did not display chemical bonding between g-C_3N_4 and AC. This results support evidence from previous observations [27].

The FTIR spectra of the spent catalysts (Fig. 4) shows that the characteristic peaks of the g-C_3N_4 and g-C_3N_4/AC composites remained unchanged after adsorption-photocatalytic degradation process. However, there is a small peak observed at around 2343–2346 cm^{-1} which represents the presence of O=C=O. This indicates that the organic compounds in the chicken processing wastewater were oxidized and formed CO_2 [42]. The occurrence of the small peak at around 1040 cm^{-1} was attributed to the presence of the orthophosphate group (PO_4^{3-}). This shows that orthophosphate was successfully adsorbed onto the surface of the composites after the adsorption-photocatalytic degradation of chicken processing wastewater. The additional peaks appearing for 60 wt% g-C_3N_4/AC at 1157.97 cm^{-1}, 1458.28 cm^{-1} and 1740.41 cm^{-1} were ascribed to C-O, C-H and C=O bending, respectively. While the peaks around 2500-3000 cm^{-1} confirmed the presence of C-H stretch [43]. These peaks corresponded to the strong adsorption of organic substances in chicken processing wastewater such as blood, flesh and fat onto the surface of 60 wt% g-C_3N_4/AC. This corroborates the COD adsorption efficiency in Fig. 7 in which a higher COD adsorption capacity was obtained by 60 wt% g-C_3N_4/AC.

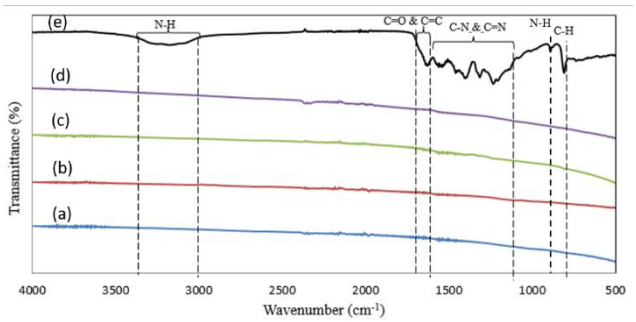

Fig. 3. FTIR spectra of (a) 20 wt% g-C_3N_4/AC, (b) 40 wt% g-C_3N_4/AC, (c) 60 wt% g-C_3N_4/AC, (d) AC and (e) g-C_3N_4 before chicken processing wastewater treatment.

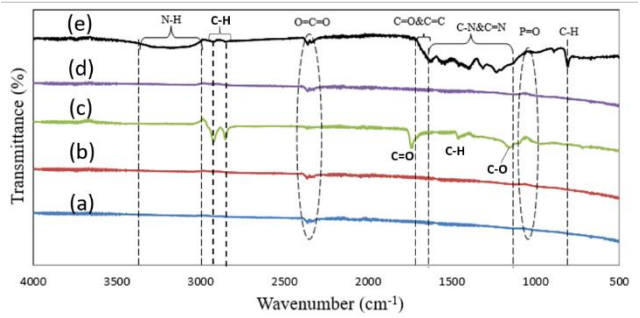

Fig. 4. FTIR spectra of (a) 20 wt% g-C_3N_4/AC, (b) 40 wt% g-C_3N_4/AC, (c) 60 wt% g-C_3N_4/AC, (d) AC and (e) g-C_3N_4 after chicken processing wastewater treatment.

3.3. Scanning electron microscopy (SEM) and energy dispersive X-ray (EDX)

From Fig. 5(a), it was observed that g-C_3N_4 had a wrinkled surface with an average particle size of 1-3 μm. However, it agglomerated and displayed an irregular lamellar structure. The g-C_3N_4 possessed a larger pore size, and this was supported by BET analysis showing that the pore size of g-C_3N_4 was 25.3242 nm (mesoporous structure). The microporous structure of AC was clearly seen in Fig. 5(b) which was consistent with its high specific surface area (1144.7041 m^2/g) and pore size of 1.9831 nm. Figs. 5(c) to (e) show that the surface morphological structure of all g-C_3N_4/AC composites was rougher than g-C_3N_4. Activated carbon which had a larger surface area could act as a support for the dispersion of g-C_3N_4 to prevent the self-aggregation of g-C_3N_4. This statement was supported by the larger specific surface area found on g-C_3N_4/AC composites compared to that of g-C_3N_4. Table 2 shows the presence of C, N and O element in g-C_3N_4 and g-C_3N_4/AC composites. The C and N element was originated from g-C_3N_4 while the detection of O element was due to the oxidation of urea during pyrolysis. There was a small percentage of N element detected in the composites due to the low yield rate of urea to g-C_3N_4. The N element increased with the increasing of weight percentage of g-C_3N_4 in the composite. In addition, there was only C and O elements detected in the AC.

Table 2. Elemental composition of the synthesized samples.

Catalyst	Elemental Composition (At. %)		
	C	N	O
AC	96.72	-	3.28
Pure g-C_3N_4	62.21	32.70	5.09
20 wt% g-C_3N_4/AC	91.17	1.01	7.81
40 wt% g-C_3N_4/AC	90.47	1.25	8.29
60 wt% g-C_3N_4/AC	95.02	2.35	2.63

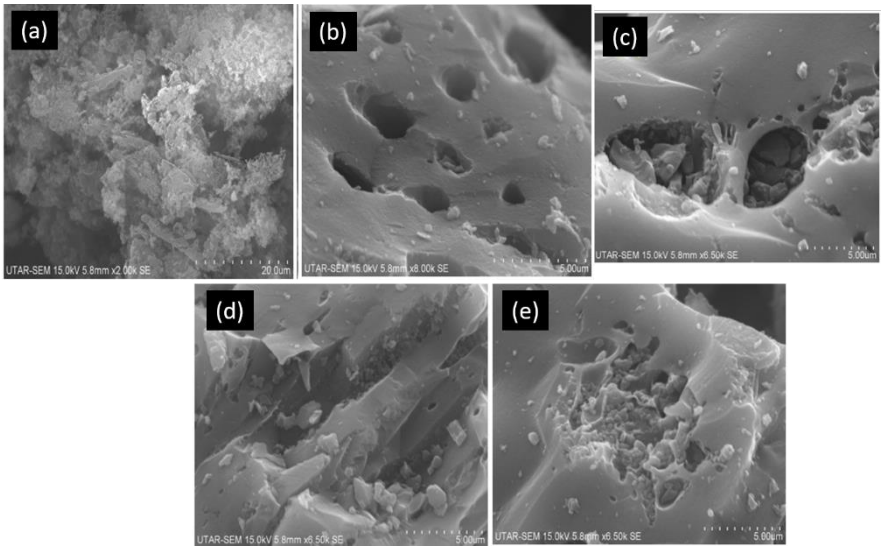

Fig. 5. SEM image of (a) g-C_3N_4, (b) AC, (c) 20 wt% g-C_3N_4/AC, (d) 40 wt% g-C_3N_4/AC, and (e) 60 wt% g-C_3N_4/AC.

3.4. X-ray diffraction (XRD)

The characteristic peaks of g-C_3N_4 were observed at around 12.9° and 27.3° in Fig. 6. A weak peak at 12.9° with the interplanar spacing of 0.688 nm was attributed to the (1 0 0) plane structural packing motif of tri-s-triazine units. Meanwhile, a strong and sharp peak at 27.3° with interplanar spacing of 0.326 nm revealed the presence of (0 0 2) lattice plane of the stacking graphitic aromatic (C-N) compounds [44, 45]. The extent of the graphitization could be determined by the sharpness of the (0 0 2) interlayer-stacking peak. It indicates that the carbon nitride was exhibited in a more graphitic nature as compared to the normal polymer-based carbon [46]. The AC exhibited two characteristic peaks at around 24.9° and 44.1° which reveal the existence of graphitic structure corresponding to (0 0 2) and (1 0 0) planes, respectively [47, 48]. All g-C_3N_4/AC composites displayed broad peaks at 25.0° and 44.0° which was mainly attributed to the graphitic structure in AC. The intensity of g-C_3N_4 characteristic peak was insignificant for g-C_3N_4/AC, implying the reduction of crystallization and polymerization of the composites [49]. It could be also due to the lower amount of g-C_3N_4 in the composites.

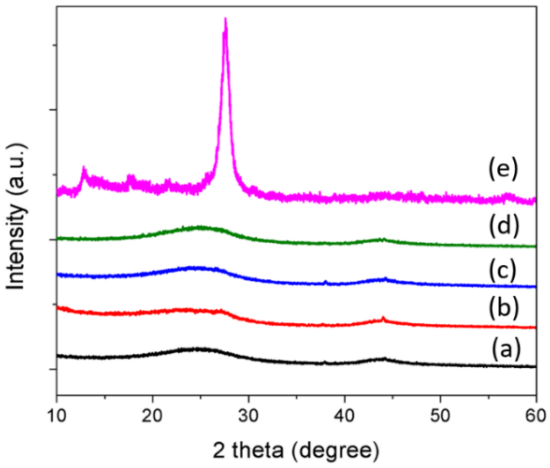

Fig. 6. XRD patterns of (a) AC, (b) 20 wt% g-C_3N_4/AC, (c) 40 wt% g-C_3N_4/AC, (d) 60 wt% g-C_3N_4/AC and (e) g-C_3N_4.

3.5. Adsorption-photocatalytic degradation of chicken processing wastewater

3.5.1. COD removal

Figure 7(a) shows that AC achieved the highest COD removal efficiency in the dark adsorption, indicating that AC removed up to 79 % of organic compounds in the chicken processing wastewater. The achievement of the highest COD removal efficiency by AC in the dark adsorption was attributed to its highest specific surface area (1144.7041 m^2/g) which adsorbed more organic compounds onto its surface. Overall, the COD removal efficiency of the synthesized catalyst in dark adsorption follows the sequence of AC (79.00 %) > 60 wt% g-C_3N_4/AC (66.90 %) > 40 wt% g-C_3N_4/AC (62.10 %) > g-C_3N_4 (34.50 %) > 20 wt% g-C_3N_4/AC (25.30 %). As shown in Fig. 7(c), both of 40 wt% g-C_3N_4/AC and 60 wt% g-C_3N_4/AC exhibited higher COD removal performance than that of g-C_3N_4 in the dark adsorption because they had higher specific surface area compared to other catalysts. Thus,

more organic compounds could be adsorbed onto the surface of the composites. In comparison with 40 wt% g-C_3N_4/AC, 60 wt% g-C_3N_4/AC exhibited a higher COD removal efficiency owing to its micropore size diameter (1.9777 nm) which was more favourable for the adsorption of organic compounds. However, 20 wt% g-C_3N_4/AC demonstrated the lowest COD removal efficiency in the dark adsorption which could be due to the lattice deformation of carbon nitride [50]. The COD removal efficiency by photocatalytic degradation follows the trend of 20 wt% g-C_3N_4/AC (47.00 %) > g-C_3N_4 (40.60 %) > 60 wt% g-C_3N_4/AC (31.30 %) > 40 wt% g-C_3N_4/AC (13.40 %) > AC (11.90 %) > blank (0.10 %) (Fig. 6(b)). The significantly enhanced photocatalytic efficiency of g-C_3N_4 (40.60 %) was attributed to the promotion of visible-light harvesting. Photocatalytic performance of 40 wt% g-C_3N_4/AC and 60 wt% g-C_3N_4/AC were poorer than that of 20 wt% g-C_3N_4/AC due to the higher loading of g-C_3N_4 which might lead to the saturation of the number of photos and light blockage [51]. Hence, the photoactivity was gradually reduced on the active sites of g-C_3N_4 and hampered the photocatalytic performance of 40 wt% g-C_3N_4/AC and 60 wt% g-C_3N_4/AC.

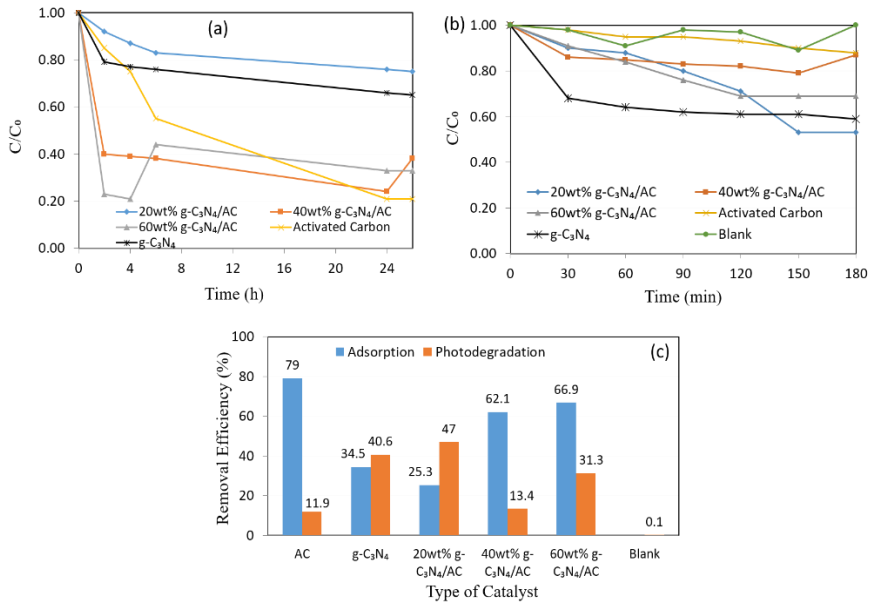

Fig. 7. (a) COD removal efficiency by (a) dark adsorption, (b) photocatalytic degradation and (c) comparison bar chart for adsorption-photocatalytic degradation of chicken processing wastewater.

3.5.2. Orthophosphate removal

As shown in Figs. 8(a) to (c), the orthophosphate removal efficiency by dark adsorption follows the sequence of g-C_3N_4 (49.10 %) > AC (28.30 %) > 40 wt% g-C_3N_4/AC (27.90 %) > 60 wt% g-C_3N_4/AC (15.40 %) > 20 wt% g-C_3N_4/AC (10.70 %). Meanwhile, the orthophosphate removal efficiency by photocatalytic degradation follows the sequence of g-C_3N_4 (49.00 %) > 40 wt% g-C_3N_4/AC (16.10 %) > AC (13.90 %) > 20 wt% g-C_3N_4/AC (12.00 %) > 60 wt% g-C_3N_4/AC (7.60 %) > Blank (1.10 %). These results suggest that g-C_3N_4 reached the highest orthophosphate

removal efficiency in the dark adsorption (49.10 %) and photodegradation (49.00 %) compared to other catalysts. The pore size of g-C_3N_4 was 25.3242 nm (Table 1) which was larger than 10 nm. Such mesoporous structure was beneficial for the advancement of orthophosphate's adsorption rate [52]. The AC could only remove 28.30 % of orthophosphate in the dark adsorption because its pore size (1.9831 nm) were too small for the orthophosphate ions (PO_4^{3-}) to be adsorbed onto its micropores. Similar observation was reported by other researchers [52, 53].

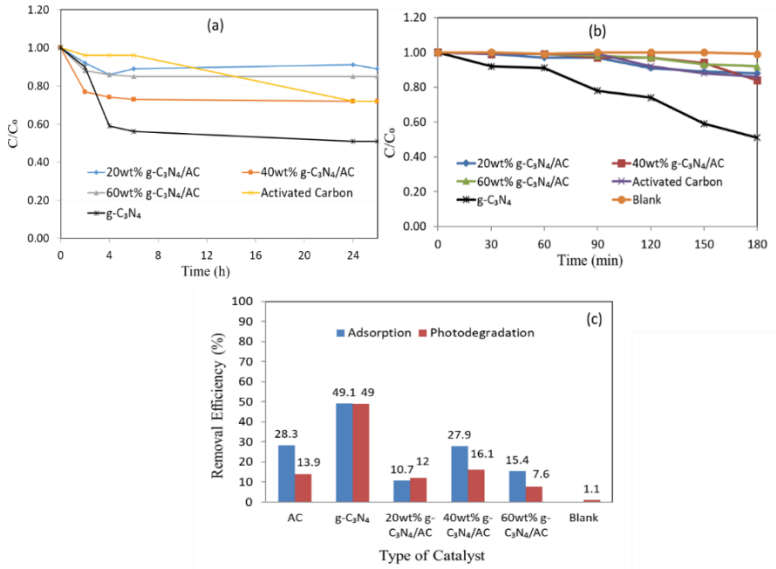

Fig. 8. (a) Orthophosphate removal efficiency by (a) dark adsorption, (b) photocatalytic degradation and (c) comparison bar chart for adsorption-photocatalytic degradation of chicken processing wastewater.

Despite of electrostatic repulsion of PO_4^{3-}, adsorption of small quantities of PO_4^{3-} could still occur due to the protonation of incomplete condensation of the amino groups on the surface of g-C_3N_4 in aqueous suspension. The existence of the deformation mode of N–H is shown at 890 cm^{-1} in FTIR. The interaction between the amine groups (CNH_2, C_2NH) with hydrogen ions and hydroxyl ions resulted in the formation of the respective positively and negatively charged amine groups [54]. The negative zeta potential of g-C_3N_4 (-17.30 mV) and 60 wt% g-C_3N_4/AC (-8.40 mV) caused the electrostatic repulsion of PO_4^{3-}. However, small quantity of PO_4^{3-} could still be adsorbed owing to the electrostatic attraction between the protonated amine groups and PO_4^{3-}. It was noticeable that the g-C_3N_4/AC composites did not show significant improvement in the dark adsorption of orthophosphate, although the incorporation of AC enhanced the specific surface area of g-C_3N_4. The average pore size of the g-C_3N_4/AC composites were less than 2 nm (Table 1) which are of microporous structure and thus, the pore size was not large enough to allow the adsorption of PO_4^{3-}. This resulted in the trivial improvement of photocatalytic performance.

3.5.3. Ammonia nitrogen removal

As shown in Figs. 9(a) to (c), the NH_3-N removal efficiency by dark adsorption follows the sequence of g-C_3N_4 (100 %) > 40 wt% g-C_3N_4/AC (60.00 %) > AC

(50.00 %) > 20 wt% g-C_3N_4/AC (34.60 %) > 60 wt% g-C_3N_4/AC (29.20 %). In comparison to orthophosphate removal, all samples displayed a better adsorption capacity towards positively ammonium ions (NH_4^+). This is because all samples possess negative zeta potential which helps to promote the adsorption of NH_4^+ through the electrostatic attraction. The zeta potential of AC, g-C_3N_4 and 60 wt% g-C_3N_4/AC is -55.30 mV, -17.30 mV and -8.40 mV, respectively. Among these samples, g-C_3N_4 was able to remove up to 100 % of NH_3-N in the dark adsorption. Among the composites, 40 wt% g-C_3N_4/AC demonstrated the highest NH_3-N removal efficiency (60.00 %) in the dark adsorption. Oxidation during pyrolysis process increased electronegative oxygen surface group on 40 wt% g-C_3N_4/AC (8.29 %) (Table 2) and thus promoting the electrostatic attraction between the positively ammonium ions (NH_4^+) and electronegative oxygen surface group. For the photocatalytic degradation performance (Fig. 9(b)), 60 wt% g-C_3N_4/AC exhibited the highest NH_3-N removal efficiency (52.90 %), followed by AC (40.00 %), 20 wt% g-C_3N_4/AC (34.00 %), 40 wt% g-C_3N_4/AC (12.50 %) and the blank (5.30 %). In this case, the photocatalytic degradation rate of NH_3-N was highly dependent on the adsorption capacity of NH_3-N onto the surface of the composite. Obviously, the higher adsorption capacity of NH_3-N could lead to a lower degradation efficiency because the active sites of composite was saturated with NH_3-N. Hence, the photonic efficiency was reduced and the photocatalyst was deactivated [55]. The overall performance of the prepared composites for chicken processing wastewater treatment under the dark adsorption and photocatalytic degradation is summarized in Table 3. It summarizes that integrated adsorption-photocatalytic degradation successfully removed 98.20 %, 98.10 % and 100% of COD, orthophosphate and NH_3-N, respectively. This work provides a feasible solution for on-site chicken processing wastewater treatment in the wet market.

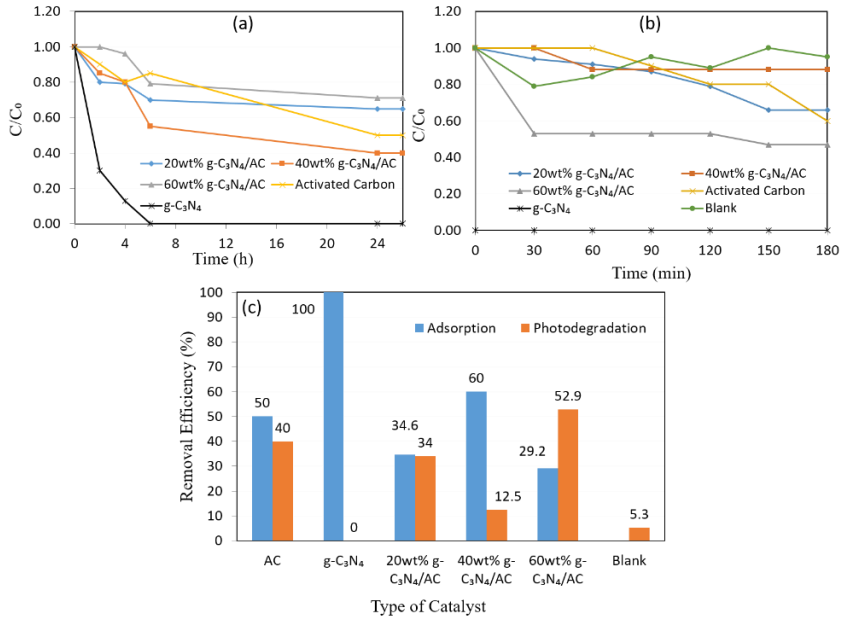

Fig. 9. (a) Ammonia nitrogen removal efficiency by (a) dark adsorption, (b) photocatalytic degradation and (c) comparison bar chart for adsorption-photocatalytic degradation of chicken processing wastewater.

Table 3. Performance of various catalyst in chicken processing wastewater treatment.

Type of Catalyst	Parameter	Adsorption Efficiency (%)	Photodegradation Efficiency (%)	Total Removal Efficiency (%)
Blank	COD	-	0.10	0.10
	Orthophosphate	-	1.10	1.10
	NH_3-N	-	5.30	5.30
AC	COD	79.00	11.90	90.90
	Orthophosphate	28.30	13.90	42.20
	NH_3-N	50.00	40.00	90.00
g-C_3N_4	COD	34.50	40.60	75.10
	Orthophosphate	49.10	49.00	98.10
	NH_3-N	100	-	100
20 wt% g-C_3N_4/AC	COD	25.30	47.00	72.30
	Orthophosphate	10.70	12.00	22.70
	NH_3-N	34.60	34.00	68.60
40 wt% g-C_3N_4/AC	COD	62.10	13.40	75.50
	Orthophosphate	27.90	16.10	44.00
	NH_3-N	60.00	12.50	72.50
60 wt% g-C_3N_4/AC	COD	66.90	31.30	98.20
	Orthophosphate	15.40	7.60	23.00
	NH_3-N	29.20	52.90	82.10

4. Conclusions

In summary, the g-C_3N_4/AC composites with different loading of g-C_3N_4 (20 wt%, 40 wt% and 60 wt%) were successfully synthesized via pyrolysis of urea and activated carbon mixture.

In the presence of AC, all g-C_3N_4/AC composites exhibited a higher specific surface area with average pore size of ~ 1.96 nm. 20 wt% g-C_3N_4/AC, g-C_3N_4 and 60 wt% g-C_3N_4/AC demonstrated the highest photodegradation efficiency for COD (47.00 %), orthophosphate (49.00 %) and NH_3-N (52.90 %).

AC achieved the highest adsorption efficiency for COD at 79% and g-C_3N_4 displayed exceptional effectiveness in adsorbing orthophosphate (49.1%) and NH_3-N (100%). The microporous structure contributed significantly to the enhancement of adsorption capacity towards COD but the excessive loading of g-C_3N_4 (40 wt% and 60 wt%) reduced the photodegradation of COD.

The microporous structure did not facilitate the enhancement of orthophosphate removal. The increased adsorption capacity of NH_3-N in 40 wt% g-C_3N_4/AC (60 %) subsequently contributed to a reduction in photocatalytic performance (12.5 %).

Overall, 98.20 % of COD, 98.10 % of orthophosphate and 100% of NH_3-N was successfully removed using integrated adsorption-photocatalytic degradation. The total removal efficiency of both COD and NH_3-N consistently displayed a good corelation with the amount of g-C_3N_4 employed.

Acknowledgement

The research has been carried out under Fundamental Research Grant Scheme project FRGS/1/2023/TK08/UTAR/02/8 provided by Ministry of Higher Education of Malaysia.

Nomenclatures

C_0	Initial concentration of pollutant, mg/L
C_t	Concentration of pollutant after adsorption / photocatalysis, mg/L
D_{pore}	Pore size, nm
S_{BET}	BET specific surface area, m^2/g
V_{tot}	Pore volume, cm^3/g

Abbreviations

AC	Powdered Activated Carbon
BET	Brunauer-Emmett-Teller
BOD	Biological Oxygen Demand
COD	Chemical Oxygen Demand
EDX	Energy Dispersive X-Ray
FTIR	Fourier Transform Infrared
g-C_3N_4	Graphitic Carbon Nitride
NH_3-N	Ammoniacal nitrogen
rGO	Reduced Graphene Oxide
SEM	Scanning Electron Microscopy
SnO_2	Tin(IV) Oxide
TiO_2	Titanium Dioxide
TN	Total Nitrogen
TP	Total Phosphorus
UV	Ultraviolet
WO_3	Tungsten(VI) Oxide
XRD	X-Ray Diffraction
ZnO	Zinc Oxide

References

1. Basitere, M.; Njoya, M.; Rinquest, Z.; Ntwampe, S.K.O.; and Sheldon, M.S. (2019). Performance evaluation and kinetic parameter analysis for static granular bed reactor (SGBR) for treating poultry slaughterhouse wastewater at mesophilic condition. *Water Practice and Technology*, 14(2), 259-268.
2. Zhan, Y.; Zhang, Z.; Ma, T.; Zhang, X.; Wang, R.; Liu, Y.; Sun, B.; Xu, T.; Ding, G.; Wei, Y.; and Li, J. (2021). Phosphorus excess changes rock phosphate solubilization level and bacterial community mediating phosphorus fractions mobilization during composting. *Bioresource Technology*, 337, 125433.
3. Njoya, M.; Basitere, M.; and Ntwampe, S.K.O. (2019). Analysis of the characteristics of poultry slaughterhouse wastewater (PSW) and its treatability. *Water Practice and Technology*, 14(4), 959-970.
4. Crini, G.; and Lichtfouse, E. (2019). Advantages and disadvantages of techniques used for wastewater treatment. *Environmental Chemistry Letters*, 17(1), 145-155.
5. Goutam, S.P.; Saxena, G.; Singh, V.; Yadav, A.K.; Bharagava, R.N.; and Thapa, K.B. (2018). Green synthesis of TiO_2 nanoparticles using leaf extract of *Jatropha curcas L.* for photocatalytic degradation of tannery wastewater. *Chemical Engineering Journal*, 336, 386-396.

6. He, S.; Hou, P.; Petropoulos, E.; Feng, Y.; Yu, Y.; Xue, L.; and Yang, L. (2018). High efficient visible-light photocatalytic performance of Cu/ZnO/rGO nanocomposite for decomposing of aqueous ammonia and treatment of domestic wastewater. *Frontiers in Chemistry*, 6, 219.
7. Li, H.; Cao, Y.; Liu, P.; Li, Y.; Zhou, A.; Ye, F.; Xue, S.; and Yue, X. (2022). Ammonia-nitrogen removal from water with g-C_3N_4-rGO-TiO_2 Z-scheme system via photocatalytic nitrification-denitrification process. *Environmental Research*, 205, 112434.
8. Dong, S.; Feng, J.; Fan, M.; Pi, Y.; Hu, L.; Han, X.; Liu, M.; Sun, J..; and Sun, J. (2015). Recent developments in heterogeneous photocatalytic water treatment using visible light responsive photocatalysis: a review. *RSC Advances*, 5, 14610-14630.
9. Sansenya, T.; Masri, N.; Chankhanittha, T.; Senasu, T.; Piriyanon, J.; Mukdasai, S.; and Nanan, S. (2022). Hydrothermal synthesis of ZnO photocatalyst for detoxification of anionic azo dyes and antibiotic. *Journal of Physics and Chemistry of Solids*, 160, 110353.
10. Zhang, J.; Lei, Y.; Cao, S.; Hu, W.; Piao, L.; and Chen, X. (2022). Photocatalytic hydrogen production from seawater under full solar spectrum without sacrificial reagents using TiO_2 nanoparticles. *Nano Research*, 15(3), 2013-2022.
11. Shandilya, P.; Sambyal, S.; Sharma, R.; Mandyal, P.; and Fang, B. (2022). Properties, optimized morphologies, and advanced strategies for photocatalytic applications of WO_3 based photocatalysts. *Journal of Hazardous Materials*, 428, 128218.
12. Sayadi, M.H.; Ghollasimood, S.; Ahmadpour, N.; and Homaeigohar, S. (2022). Biosynthesis of the ZnO/SnO_2 nanoparticles and characterization of their photocatalytic potential for removal of organic water pollutants. *Journal of Photochemistry and Photobiology A: Chemistry*, 425, 113662.
13. Hu, S.; Jin, R.; Lu, G.; Liu, D.; and Gui J. (2014). The properties and photocatalytic performance comparison of Fe^{3+} doped g-C_3N_4 and Fe_2O_3/g-C_3N_4 composite catalysts. *RSC Advances*, 4, 24863-24869.
14. Wang, X.; Maeda, K.; Thomas, A.; Takanabe, K.; Xin, G.; Carlsson, J.M.; Domen, K.; and Antonietti, M. (2009). A metal-free polymeric photocatalyst for hydrogen production from water under visible light. *Nature Materials*, 8(1), 76-80.
15. Kumar, S.; T, S.; Kumar, B.; Baruah, A.; and Shanker, V. (2013). Synthesis of magnetically separable and recyclable g-C_3N_4-Fe_3O_4 hybrid nanocomposites with enhanced photocatalytic performance under visible light irradiation. *The Journal of Physical Chemistry C*, 117, 26135-26143.
16. Sim, L.C.; Tai, J.Y.; Leong, K.H.; Saravanan, P.; Tan, S.T.; Chong, W.C.; and Abd Aziz, A. (2021). Metal free and sunlight driven g-C_3N_4 based photocatalyst using carbon quantum dots from Arabian dates: Green strategy for photodegradation of 2, 4-dichlorophenol and selective detection of Fe^{3+}. *Diamond and Related Materials*, 120, 108679.
17. Mohamed, N.A.; Ullah, H.; Safaei, J.; Ismail, A.F.; Mohamad Noh, M.F.; Soh, M.F.; Ibrahim, M.A.; Ludin, N.A.; and Mat Teridi, M.A. (2019). Efficient photoelectrochemical performance of γ irradiated g-C_3N_4 and its g-

C_3N_4@$BiVO_4$ heterojunction for solar water splitting. *The Journal of Physical Chemistry C*, 123(14), 9013-9026.

18. Wang, C.; Zhao, Y.; Xu, H.; Li, Y.; Wei, Y.; Liu, J.; and Zhao, Z. (2020). Efficient Z-scheme photocatalysts of ultrathin g-C_3N_4-wrapped Au/TiO_2-nanocrystals for enhanced visible-light-driven conversion of CO_2 with H_2O. *Applied Catalysis B: Environmental*, 263, 118314.
19. Liu, X.; Wang, Q.; Chen, J.; Chen, X.; and Yang, W. (2021). Ultrasensitive electrochemiluminescence biosensor for the detection of tumor exosomes based on peptide recognition and luminol-AuNPs@ g-C_3N_4 nanoprobe signal amplification. *Talanta*, 221, 121379.
20. Tran Huu, H.; Thi, M.D.N.; Nguyen, V.P.; Thi, L.N.; Phan, T.T.T.; Hoang, Q.D.; Luc, H.H.; Kim, S.J.; and Vo, V. (2021). One-pot synthesis of S-scheme MoS_2/g-C_3N_4 heterojunction as effective visible light photocatalyst. *Scientific Reports*, 11(1), 14787.
21. Wang, Y.; Jia, H.; Gong, H.; Zhou, L.; Qiu, Z.; Fang, X.; and Du, T. (2021). Fabrication of trimodal porous silica/g-C_3N_4 nanotubes for efficient visible light photocatalytic reduction of CO_2 to ethanol. *Chemical Engineering Journal*, 426, 130877.
22. Aanchal; Barman, S.; and Basu, S. (2020). Complete removal of endocrine disrupting compound and toxic dye by visible light active porous g-C_3N_4/H-ZSM-5 nanocomposite. *Chemosphere*, 241, 124981.
23. Du, Y.; Liu, X.; Wang, Q.; Yu, L.; Chu, L.; and Sun, M. (2022). Metal free benzothiadiazole-diketopyrrolopyrrole-based conjugated polymer/g-C_3N_4 photocatalyst for enhanced sterilization and degradation in visible to near-infrared region. *Journal of Colloid and Interface Science*, 608(1), 103-113.
24. Briche, S.; Derqaoui, M.; Belaiche, M.; El Mouchtari, E.M.; Wong-Wah-Chung, P.; and Rafqah, S. (2020). Nanocomposite material from TiO_2 and activated carbon for the removal of pharmaceutical product sulfamethazine by combined adsorption/photocatalysis in aqueous media. *Environmental Science and Pollution Research*, 27(20), 25523-25534.
25. Rodríguez-Reinoso, F. (2001). *Activated carbon and adsorption*. In Buschow, K.H.J.; Cahn, R.W.; Flemings, M.C.; Ilschner, B.; Kramer, E.J.; Mahajan, S.; and Veyssière P. (Eds.), *Encyclopedia of Materials: Science and Technology*. Elsevier.
26. Reimerink, W.M.T.M. (1999). *The use of activated carbon as catalyst and catalyst carrier in industrial applications*. In Dąbrowski, A. (Ed.), *Studies in Surface Science and Catalysis.* Elsevier.
27. Chen, X.; Kuo, D-.H.; and Lu, D. (2016). Nanonization of g-C_3N_4 with the assistance of activated carbon for improved visible light photocatalysis. *RSC Advances*, 6, 66814-66821.
28. Ao, W.; Qu, J.; Yu, H.; Liu, Y.; Liu, C.; Fu, J.; Dai, J.; Bi, X.; Yuan, Y.; and Jin, Y. (2022). TiO_2/activated carbon synthesized by microwave-assisted heating for tetracycline photodegradation. *Environmental Research*, 214(2), 113837.
29. Al Mamari, S.; Khudaish, E.; Kim, Y.; Khraisheh, M.; and Selvaraj, R. (2023). Lotus-bud like hexagonal ZnO/g-C_3N_4 composites for the photodegradation of benzene present in aqueous solution. *Inorganic Chemistry Communications*, 150, 110539.

30. Zhang, Y.; Zheng, Y.; and Yu, X. (2023). Self-assembly of two-dimensional g-C_3N_4/rGO nanojunctions with enhanced charge separation and transfer for photocatalytic H_2 production. *International Journal of Hydrogen Energy*, 48(42), 15992-16000.
31. Ismael, M. (2023). One-step ultrasonic-assisted synthesis of Ni-doped g-C_3N_4 photocatalyst for enhanced photocatalytic hydrogen evolution. *Inorganic Chemistry Communications*, 151, 110607.
32. Mergbi, M.; Aboagye, D.; Contreras, S.; Amor, H.B.; Medina, F.; and Djellabi, R. (2023). Fast g-C_3N_4 sonocoated activated carbon for enhanced solar photocatalytic oxidation of organic pollutants through Adsorb & Shuttle process. *Ultrasonics Sonochemistry*, 99, 106550.
33. Olufemi Oluwole, A.; Khoza, P.; and Olatunji, O.S. (2022). Synthesis and characterization of g-C_3N_4 doped with activated carbon (AC) prepared from grape leaf litters for the photocatalytic degradation of enrofloxacin in aqueous systems. *ChemistrySelect*, 7(45), e202203601.
34. Shoaib, A.G.M.; El-Sikaily, A.; El Nemr, A.; Mohamed, A.E.-D.A.; and Hassan, A.A. (2022). Preparation and characterization of highly surface area activated carbons followed Type IV from marine red alga (*Pterocladia capillacea*) by zinc chloride activation. *Biomass Conversion and Biorefinery*, 12, 2253-2265.
35. Wei, M.; Gao, L.; Li, J.; Fang, J.; Cai, W.; Li, X.; and Xu, A. (2016). Activation of peroxymonosulfate by graphitic carbon nitride loaded on activated carbon for organic pollutants degradation. *Journal of Hazardous Materials*, 316, 60-68.
36. Berenguer, R.; and Morallón, E. (2019). Oxidation of different microporous carbons by chemical and electrochemical methods. *Frontiers in Materials*, 6, 130.
37. Yan, S.C.; Li, Z.S.; and Zou, Z.G. (2009). Photodegradation performance of g-C_3N_4 fabricated by directly heating melamine. *Langmuir*, 25(17), 10397-10401.
38. Martín-Ramos, P.; Martín-Gil, J.; Dante, R.C.; Vaquero, F.; Navarro, R.M.; and Fierro, J.L.G. (2015). A simple approach to synthesize g-C_3N_4 with high visible light photoactivity for hydrogen production. *International Journal of Hydrogen Energy*, 40(23), 7273-7281.
39. Chen, Y..; Li, J.; Hong, Z.; Shen, B.; Lin, B.; and Gao, B. (2014). Origin of the enhanced visible-light photocatalytic activity of CNT modified g-C_3N_4 for H_2 production. *Physical Chemistry Chemical Physics*, 16(17), 8106-8113.
40. Xiang, Q.; Yu, J.; and Jaroniec, M. (2011). Preparation and enhanced visible-light photocatalytic H_2-production activity of graphene/C_3N_4 composites. *The Journal of Physical Chemistry C*, 115(15), 7355-7363.
41. Lv, S.; Li, Y.; Zhang, K.; Lin, Z.; and Tang, D. (2017). Carbon dots/g-C_3N_4 nanoheterostructures-based signal-generation tags for photoelectrochemical immunoassay of cancer biomarkers coupling with copper nanoclusters. *ACS Applied Materials and Interfaces*, 9(44), 38336-38343.
42. Diarmand-Khalilabad, H.; Habibi-Yangjeh, A.; Seifzadeh, D.; Asadzadeh-Khaneghah, S.; and Vesali-Kermani, E. (2019). g-C_3N_4 nanosheets decorated with carbon dots and CdS nanoparticles: Novel nanocomposites with excellent nitrogen photofixation ability under simulated solar irradiation. *Ceramics International*, 45(2), 2542-2555.

43. Nandiyanto, A.B.D.; Oktiani, R.; and Ragadhita, R. (2019). How to read and interpret FTIR spectroscope of organic material. *Indonesian Journal of Science and Technology*, 4(1), 97-118.
44. Manimozhi, R.; Mathankumar, M.; and Gnana Prakash, A.P. (2021). Synthesis of g-C_3N_4/ZnO heterostructure photocatalyst for enhanced visible degradation of organic dye. *Optik*, 229, 165548.
45. Hu, C.; Chen, F.; Wang, Y.; Tian, N.; Ma, T.; Zhang, Y.; and Huang, H. (2021). Exceptional cocatalyst-free photo-enhanced piezocatalytic hydrogen evolution of carbon nitride nanosheets from strong in-plane polarization. *Advanced Materials*, 33(24), 2101751.
46. Hwang, S.; Lee, S.; and Yu, J.-S. (2007). Template-directed synthesis of highly ordered nanoporous graphitic carbon nitride through polymerization of cyanamide. *Applied Surface Science*, 253(13), 5656-5659.
47. Babu Rajendran, A.; Manivannan, G.; Jothivenkatachalam, K.; and Karthikeyan, S. (2015). Characterization studies of activated carbon from low cost agricultural waste: *leucaena leucocephala* seed shell. *RASĀYAN Journal of Chemistry*, 8(3), 330-338.
48. Omri, A.; and Benzina, M. (2012). Characterization of activated carbon prepared from a new raw lignocellulosic material: *Ziziphus spina-christi* seeds. *Journal de la Société Chimique de Tunisie*, 14, 175-183.
49. Fang, S.; Xia, Y.; Lv, K.; Li, Q.; Sun, J.; and Li, M. (2015). Effect of carbon dots modification on the structure and photocatalytic activity of g-C_3N_4. *Applied Catalysis B: Environmental*, 185, 225-232.
50. Benesi, H.A. (1957). Acidity of catalyst surfaces. II. Amine titration using Hammett indicators. *The Journal of Physical Chemistry*, 61(7), 970-973.
51. Zhang, D.; Lv, S.; and Luo, Z. (2020). A study on the photocatalytic degradation performance of a $[KNbO_3]_{0.9}$-$[BaNi_{0.5}Nb_{0.5}O_{3-\delta}]_{0.1}$ perovskite. *RSC Advances*, 10(3), 1275-1280.
52. Suresh Kumar, P.; Korving, L.; Keesman, K.J.; van Loosdrecht, M.C.M.; and Witkamp, G.-J. (2019). Effect of pore size distribution and particle size of porous metal oxides on phosphate adsorption capacity and kinetics. *Chemical Engineering Journal*, 358, 160-169.
53. Zhang, L.; Chen, Z.; and Zhao, Y-.L. (2019). *Well production performance analysis for shale gas reservoirs*. Elsevier.
54. Zhu, B.; Xia, P.; Ho, W.; and Yu, J. (2015). Isoelectric point and adsorption activity of porous g-C_3N_4. *Applied Surface Science*, 344, 188-195.
55. Saquib, M.; and Muneer, M. (2003). TiO_2-mediated photocatalytic degradation of a triphenylmethane dye (gentian violet), in aqueous suspensions. *Dyes and Pigments*, 56(1), 37-49.